Using specularity content to evaluate eight geothermal heat flow maps of Totten Glacier

Yan Huang[1]，Liyun Zhao[1*], Yiliang Ma[1], Michael Wolovick[2], John C. Moore[1,3*]

[1] State Key Laboratory of Earth Surface Processes and Resource Ecology, Faculty of Geographical Science, Beijing Normal University, Beijing 100875, China

[2] Glaciology Section, Alfred-Wegener-Institut Helmholtz-Zentrum für Polar- und Meeresforschung, Bremerhaven, Germany

[3] Arctic Centre, University of Lapland, Rovaniemi, Finland

* Corresponding author

Corresponding author: Liyun Zhao (zhaoliyun@bnu.edu.cn); John C. Moore (john.moore.bnu@gmail.com)

Abstract

Geothermal heat flow (GHF) is the dominant factor affecting the basal thermal regime of ice sheet dynamics. But it is poorly defined for the Antarctic ice sheet. We compare basal thermal state of the Totten Glacier catchment as simulated by eight different GHF datasets. We use a basal energy and water flow model coupled with a 3D full-Stokes ice dynamics model to estimate the basal temperature, basal friction heat and basal melting rate. In addition to the location of subglacial lakes, we use specularity content of the airborne radar returns as a two-sided constraint to discriminate between local wet or dry basal conditions and compare them with the basal state simulations with different GHF. Two medium magnitude GHF distribution maps derived from seismic modelling rank well at simulating both cold and warm bed regions, the GHFs from Shen et al. (2020) and Shapiro and Ritzwoller (2004). The best-fit simulated result shows that most of the inland bed area is frozen. Only the central inland subglacial canyon, co-located with high specularity content, reaches pressure-melting point consistently in all the eight GHFs. Modelled basal melting rates in the slow-flowing region are generally 0-5 mm yr^{-1} but with local maxima of 10 mm yr^{-1} at the central inland subglacial canyon. The fast-flowing grounded glaciers close to Totten ice shelf are lubricating their bases with melt water at rates of 10-400 mm yr^{-1}.

1 Introduction

Totten Glacier is the primary outlet glacier of the Aurora Subglacial Basin (ASB; Fig. 1), and one of the most vulnerable glaciers to a warming climate in East Antarctica (Li et al., 2016; Dow et al., 2020). It holds an ice volume equivalent to 3.9 meters of global sea level rise (Morlighem et al., 2020; Greenbaum et al., 2015). Most of the bedrock below Totten Glacier is below sea level. The floating part, Totten Ice Shelf has a relatively high basal melt rate of ~10 m yr^{-1} compared with other ice shelves in East Antarctica (Rignot et al., 2013, Roberts et al., 2018) and has thinned and lost mass rapidly in recent years (Pritchard et al., 2009; Adusumilli et al., 2020).

The ASB has a widespread distributed hydrological network with almost 200 'lake-like'

or water accumulation features (Wright et el., 2012; Livingstone et al., 2022). There may be a hydrological flow pathway operating from subglacial lakes near the Dome C ice divide and the coast via the Totten Glacier (Wright et al., 2012), potentially affecting the stability of the Totten Glacier.

Basal melting contribute to subglacial hydrological flow. Basal meltwater lubricates the flow of ice, which can impact the stability of the ice sheet and the direction of the ice flow (Livingstone et al., 2016; Bell et al., 2007). The basal meltwater moves down the pressure gradient and gradually develops into a complex subglacial hydrological system, which eventually flows into the ocean (Fricker et al., 2016). However, the spatial structure of the basal thermal state and basal melting rates beneath the Totten Glacier are not yet well understood.

Basal melting can occur where the ice temperature reaches the pressure melting point, dramatically lowering the basal friction and allowing the ice to flow faster. Geothermal heat flow (GHF) is a key boundary condition for ice temperature. Its magnitude and distribution affect the distribution of basal ice temperature and thus the ice flow. The magnitude of GHF depends on the spatially varying geological conditions that control heat generation and conduction, including heat flow from the mantle, crustal thickness, heat production in the crust by radioactive decay, groundwater flow, and tectonic history (Pollack et al., 1993; Pittard et al., 2016; Reading et al., 2022). The bed topography affects heat diffusion pathways to the earth's crust, therefore has influence on GHF at kilometer scales. Typically, near-surface temperature gradient is decreased near topographic rises and increased near topographic depressions (Bullard, 1938; Colgan et al., 2021). It is difficult to measure GHF directly due to limited access to Antarctic bedrock, with only a few point measurements in ice-free areas or from boreholes through the ice (Fisher et al., 2015). GHF datasets are commonly estimated from models (Burton-Johnson et al., 2020) relying on either seismic models (Shapiro and Ritzwoller, 2004; An et al., 2015; Shen et al., 2020), magnetically-derived models (Martos et al., 2017; Purucker, 2012 - an update of Fox-Maule et al., 2005;), or multivariate approach (Stål et al., 2021) including machine learning (Lösing et al., 2021).

Previous thermomechanical simulations of the whole Antarctic including Totten Glacier (Dow et al., 2020; Pattyn et al., 2010; Pittard et al., 2016; Van Liefferinge and Pattyn, 2013; Van Liefferinge et al., 2018) have used GHF data from Shapiro and Ritzwoller (2004), Fox Maule et al. (2005), Purucker (2012) and An et al. (2015), but Wright et al. (2012) and Huybrechts (1990) used spatially uniform values. In this study, we simulated the basal thermal state of Totten Glacier, based on the best available topographic data and eight different GHFs, including three GHF listed above, plus more recent GHF fields from Martos et al. (2017) and Shen al et. (2020), and three latest GHF datasets from Stål et al. (2021), Lösing et al. (2021), and Haeger et al. (2022).

We apply an off-line coupling between a basal energy and water flow model and a 3D full-Stokes ice flow model for each of the eight GHF maps, to provide the best-fit

87 distribution of modelled basal temperature and basal melt rate. We evaluate the
88 simulated basal temperature fields under the different GHF maps using the observations
89 of water at the ice base to infer which GHF map is most reliable in the ASB. The
90 observations include a set of subglacial lakes locations and the specularity content (Dow
91 et al., 2020) calculated from airborne radar data collected by the International
92 Collaborative Exploration of the Cryosphere by Airborne Profiling (ICECAP) survey.
93 Specularity is a parameterization of the along-track radar bed reflection scattering
94 function that has been used to provide an attenuation-independent proxy for distributed
95 subglacial water bodies (Schroeder et al., 2013). We devise measures of specularity that
96 help discriminate between alternative GHF maps to best characterize both cold and
97 warm beds.
98
99 **2 Regional Domain and Datasets**
100 Our modeled domain, the Totten Glacier, is located in the Aurora Subglacial Basin in
101 East Antarctica (Fig. 1). Its boundary is based on drainage-basin boundaries defined
102 from satellite ice sheet surface elevation and velocities (Mouginot et al., 2017). The
103 surface elevation, bedrock elevation, and ice thickness are from MEaSUREs
104 BedMachine Antarctica, version 2 with a resolution of 500 m (Morlighem et al., 2020).
105
106 Simulation input and comparison datasets are shown in Table 1. The surface ice velocity
107 data are obtained from MEaSUREs Phase-Based Antarctica Ice Velocity Map, Version
108 2 with resolution of 450 m (Rignot et al., 2017), which were mainly collected during
109 the International Polar Years from 2007 to 2009 with additional surveys between 2013
110 and 2016. Ice sheet surface temperature is prescribed by ALBMAP v1 with a resolution
111 of 5 km (Le Brocq et al., 2010a) and comes from monthly estimates inferred from
112 AVHRR data averaged over 1982-2004 (Comiso, 2000). Subglacial lake locations are
113 from the fourth inventory of Antarctic subglacial lakes (Wright and Siegert, 2012) and
114 the first global inventory of subglacial lakes (Livingstone et al., 2022).
115
116 Eight GHF datasets (Fig. 2; Table 2) are used in this study. Martos et al. (2017) GHF
117 and Purucker (2012) GHF are both derived from magnetically-derived models, but their
118 magnitude vary significantly on a regional scale, which is mainly related to the
119 resolution of magnetic anomaly data (Burton-Johnson et al., 2020). Shapiro and
120 Ritzwoller (2004), An et al. (2015), and Shen et al. (2020) all used seismic data, but
121 they used different approaches in deriving heat flow. The latest three GHF datasets, Stål
122 et al. (2021), Lösing et al. (2021), and Haeger et al. (2022), are generated based on
123 multiple observables. All the GHF datasets are bilinearly interpolated into 2.0 km
124 resolution. Then we calculated the ensemble mean and standard deviation (SD) of the
125 eight GHF maps, and a uniform GHF value, 59 mW m^{-2}, which is the area average of
126 ensemble mean (Fig. 2). The SD of 8 GHF is less than 10 mW m^{-2} over the domain.
127
128 The specularity content data are from Dow et al (2020), where they calculated radar
129 specularity content over ASB from the ICECAP survey lines, and smoothed the data
130 with a 1 km filter, following the equations described in Schroeder et al. (2015).

Specularity content is given as a relative value between 0 and 1, larger values mean a higher likelihood of water presence, and value of 0.4 is taken as the division where specularity content shows the presence of water (Young et al., 2016).

Table 1 Datasets used in simulations.

Variable name	Dataset	Resolution	Reference
surface elevation, bedrock elevation, and ice thickness	MEaSUREs BedMachine Antarctica version 2	500 m	Morlighem et al., 2020; Cui et al., 2020
surface ice velocity	MEaSUREs InSAR-based Antarctic ice velocity Map, version 2	450 m	Rignot et al., 2017
surface temperature	ALBMAP v1	5 km	Le Brocq et al., 2010a
subglacial lake location	The first global inventory of subglacial lakes	-----	Wright and Siegert, 2012; Livingstone et al., 2022
specularity content	Aurora Subglacial Basin GlaDs inputs, outputs and geophysical data	1 km along track	Dow et al., 2019
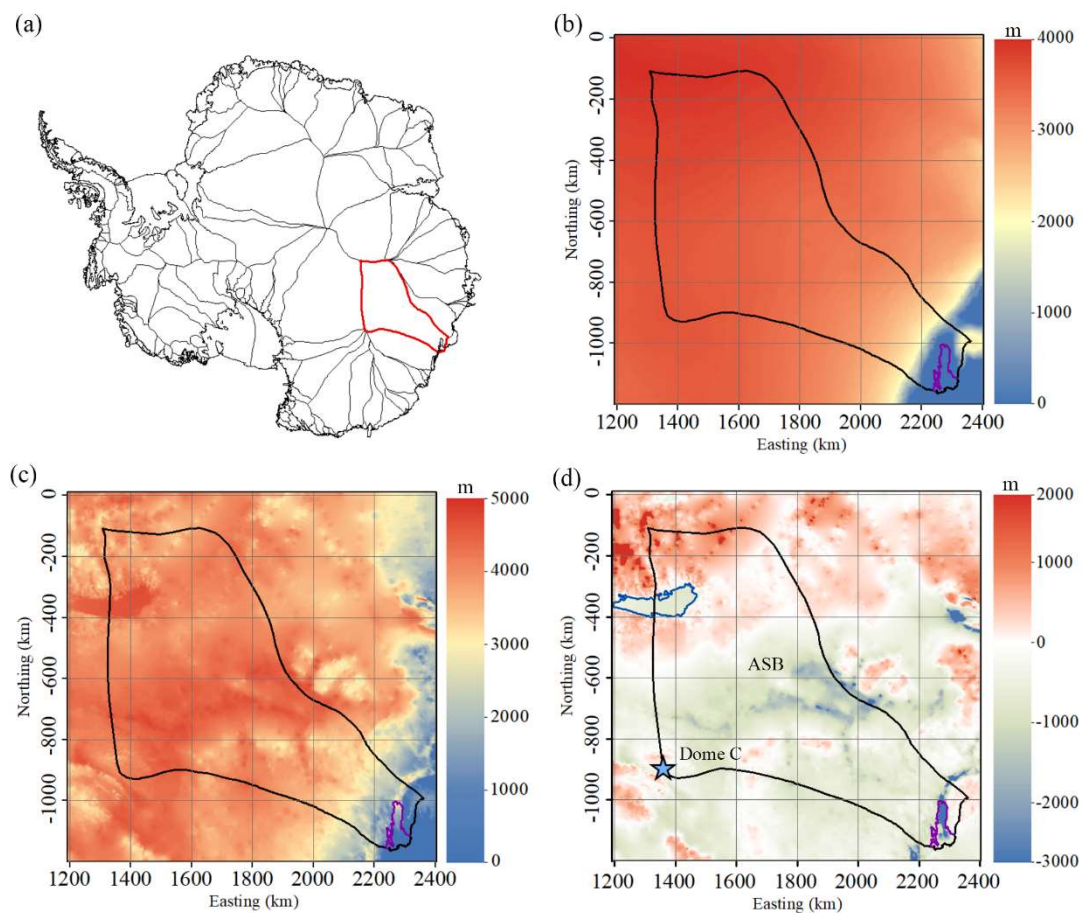
Fig. 1. (a) The location of our domain in Antarctica; (b) surface elevation; (c) ice thickness; (d) bed elevation with region boundary overlain. The solid black curve is the outline of the study domain, including the Totten ice shelf. The solid red line in (a) is the boundary of Totton Glacier. The purple line in (b-d) depicts the grounding line of Totten glacier. The blue curve in (d) depicts Lake Vostok (Studinger et al., 2003). ASB and Dome C (blue star) are marked in (d).

144

145

146   Table 2 The ten GHF maps used with the mean, range and resolution in our region.

147

GHF maps	Method	Mean (mW m^{-2})	Range (mW m^{-2})	Resolution (km)
Martos et al., 2017	airborne geomagnetic data derived model	65	51-70	15
Purucker, 2012	satellite geomagnetic data derived model	51	37-67	100-400
Shen et al., 2020	seismic model	58	42-63	100-200
An et al., 2015	seismic model	51	34-56	100-200
Shapiro and Ritzwoller, 2004	seismic model	58	44-63	~100
Stål et al., 2021	multivariate approach	60	34-80	20
Lösing et al., 2021	machine learning	63	47-71	55
Haeger et al., 2022	multivariate approach	64	54-67	10
Mean GHF	Ensemble mean of the 8 datasets above inter-polated into 2.0 km resolution	59	48-61	2
Constant GHF	mean of the ensemble mean GHF	59	59	2

148

149
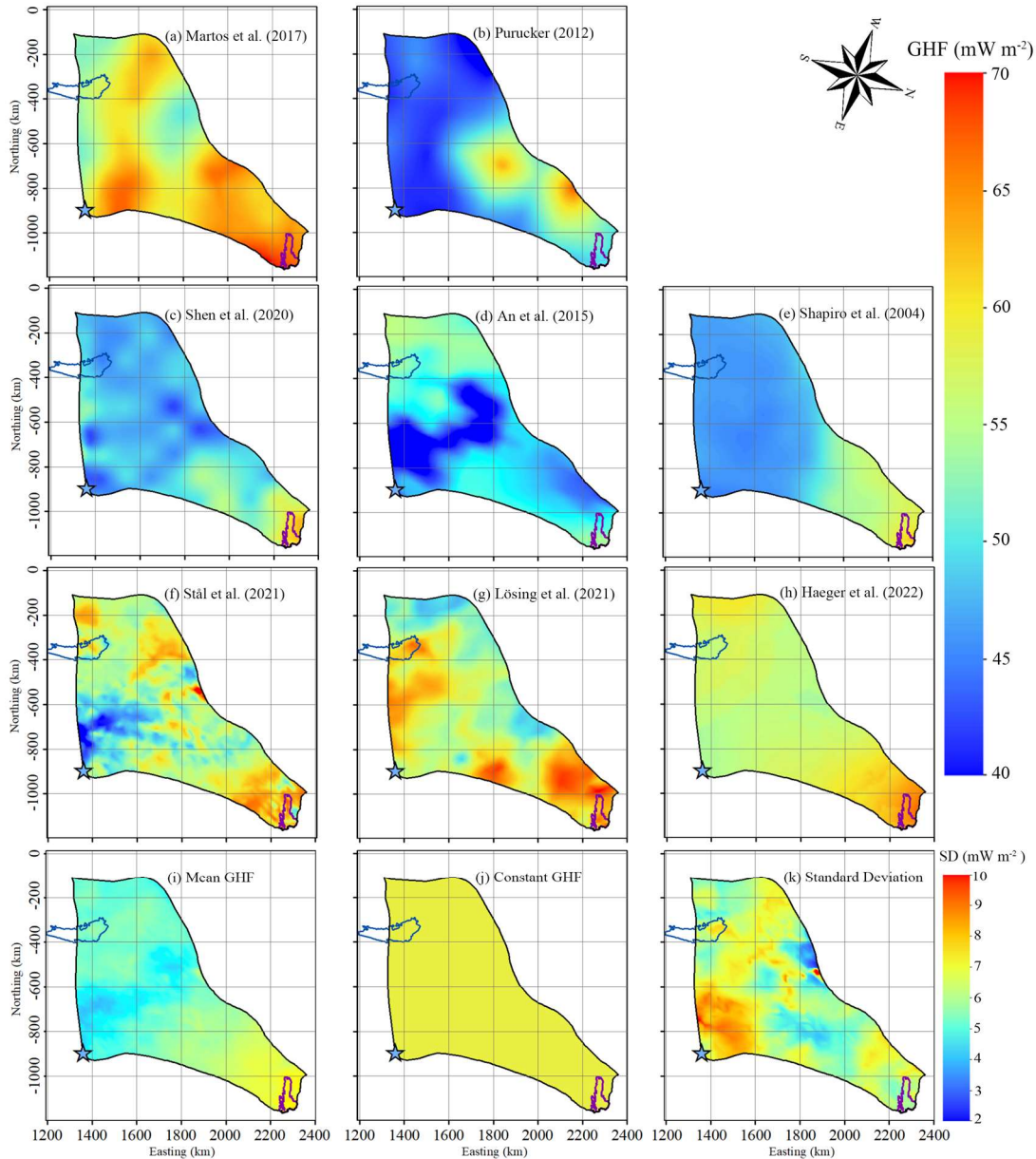
Fig. 2. The spatial distribution of GHF listed in Table 2 over our domain (a)-(j). The ensemble mean GHF and standard deviation of the 8 GHF (a)-(h) are given in (i) and (k). Panel (j) shows the constant GHF of 59 mW m^{-2}. The purple line depicts the grounding line. The blue curve depicts Lake Vostok. The blue star denotes Dome C.

3 Model

Our goal is to map the basal thermal state of Totten glacier, including basal temperature and basal melting rate. GHF, basal frictional heat and englacial heat conduction are the main factors that determine the basal thermal state of the ice sheet. We need to simulate the ice flow velocity and stress to calculate the basal frictional heat, and to simulate the ice temperature to calculate the englacial heat conduction flux.

Following the same method as Kang et al. (2022), we solve an inverse problem by a full-Stokes model, implemented in Elmer/Ice (Gagliardini et al., 2013), to infer the

basal friction coefficient such that the modelled velocity best fits observations. To get a proper vertical ice temperature profile subject to thermal boundary conditions needed in solving the inverse problem, we use a forward model that consists of an improved Shallow Ice Approximation (SIA) thermomechanical model with a subglacial hydrology model (Wolovick et al., 2021). We do steady state simulations by coupling the forward and inverse models, using 8 GHF datasets, as well as the ensemble mean GHF and a constant GHF value of 59 mW m^{-2} (Fig. 2).

3.1 Mesh Generation and Refinement

We use GMSH (Geuzaine and Remacle, 2009) to generate an initial 2-D horizontal footprint mesh. Then we refine the mesh by an anisotropic mesh adaptation code in the Mmg library (http://www.mmgtools.org/). The resulting mesh is shown in Fig. 3 and has minimum and maximum element sizes of about 800 m and 20 km. The range of mesh size is 800 m at ice shelf, 1-3 km upstream near the grounding line, and 6-20 km over most of the inland ice. The 2-D mesh is then vertically extruded using 10 equally spaced, terrain following layers.
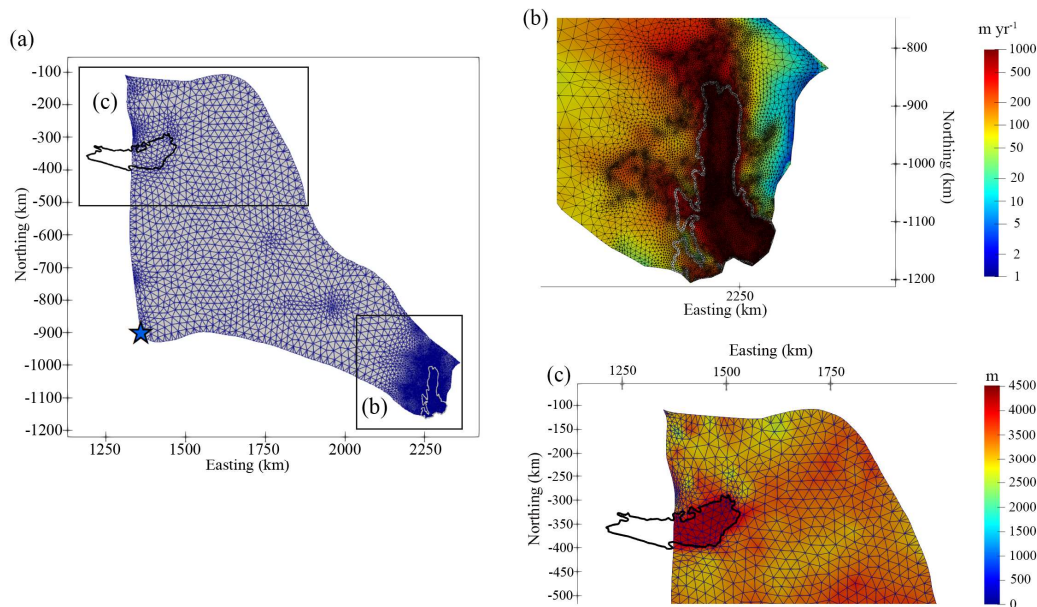
Fig. 3. The refined 2-D horizontal domain footprint mesh (a). Boxes outlined in (a) are shown in detail overlain with surface ice velocity (unit: m yr^{-1}) in (b) and with ice thickness in (c). The while line in (a) and (b) depicts the grounding line. The black curve in (a) and (c) depicts Lake Vostok. The blue star in (a) denotes Dome C.

3.2 Boundary Conditions

The ice surface is assumed to be stress-free. At the ice front, the normal stress under the sea surface is equal to the hydrostatic water pressure. On the lateral boundary, the normal stress is equal to the ice pressure applied by neighboring glaciers and the normal velocity is assumed to be 0. The bed for grounded ice is assumed to be rigid, impenetrable, and fixed over time. For simplicity, we ignore the existence of Lake

194 Vostok and replace the lake with bedrock. We do this to avoid having to implement a
195 spatially variable sea level in our model, as the level of hydrostatic equilibrium in Lake
196 Vostok is several thousand meters higher than in the ocean. Our inverted drag
197 coefficient over the lake is very low, indicating that our simplification has only a small
198 influence on ice flow. However, our basal melt rates over the lake are probably
199 inaccurate, as we assume that geothermal flux from the lake bottom is applied directly
200 to the ice base, without accounting for circulation within the lake.
201 A linear sliding law is used to describe the relationship between the basal sliding
202 velocity and the basal shear force, on the bottom of grounded ice,

$$\tau_b = C \cdot u_b, \tag{1}$$

203 To avoid non-physical negative values, $C = 10^\beta$ is used in the simulation. We call β
204 the basal friction coefficient. C is initialized to a constant value of 10^{-4} MPa m^{-1} yr
205 (Gillet-Chaulet et al., 2012), and then replaced with the inverted C in subsequent
206 inversion steps.
207
208 We relax the free surface of the domain by a short transient run to reduce the non-
209 physical spikes in initial surface geometry (Zhao et al., 2018). The transient simulation
210 period here is 0.5 yr with a timestep of 0.01 yr.
211
212 Following the same method as Kang et al. (2022), we improve the parameterization of
213 β via C in Eq 5 (Section 3.2.2) by considering basal temperature T_{bed},

$$\beta_{new} = \beta_{old} + \alpha(T_m - T_{bed}), \tag{2}$$

214 where β_{old} is from the inverse model, α is a positive factor to be tuned, T_m is pressure
215 melting temperature. We take α to be 1, and use the parameterization of β_{new} in Eq 1
216 in all the simulations (Kang et al., 2022). Using Eq 2 does not change simulated surface
217 velocities in the interior region.
218
219   **3.3 Basal Melt Rate**
220 Based on the inverted basal velocity and basal shear stress, we can calculate the basal
221 friction heat. We then produce the basal melt rate using the thermal equilibrium as
222 follows (Greve and Blatter, 2009):

$$M = \frac{G + \vec{u}_b \vec{\tau}_b + k(T)\frac{dT}{dz}}{\rho_i L}, \tag{3}$$

223 where M is the basal melt rate, G is GHF, $\vec{u}_b \vec{\tau}_b$ is the basal friction heat, $-k(T)\frac{dT}{dz}$ is the

224 upward heat conduction, ρ_i is the ice density, and L is latent heat of ice melt. GHF and

225 frictional heating from basal slip warm the base, while the upward heat conduction to
226 the interior cools the base.

4 Simulation Results

4.1 Ice Velocity

The modeled surface velocity fields with different GHFs are all very close to the observed as expected by design of the minimization of misfit between the modeled and the observed surface velocity in the inverse model. Therefore, we show only the Martos et al. (2017) result as a representative example of all simulated velocity fields (Fig. 4). The surface speed can reach as high as about 1000 m yr^{-1} on the ice shelf (Fig. 4a, b).

Fig. 4c shows the modeled basal ice velocity. The modeled basal ice velocity is close to 0 in most of the inland region. The fast basal velocity in the middle of the region (Fig. 4c) is associated with subglacial canyon features (Fig. 1c), high basal temperature (Fig. 5) and small friction coefficient. In the grounded fast flow region, the basal ice velocity can reach a maximum of 500 m yr^{-1}.
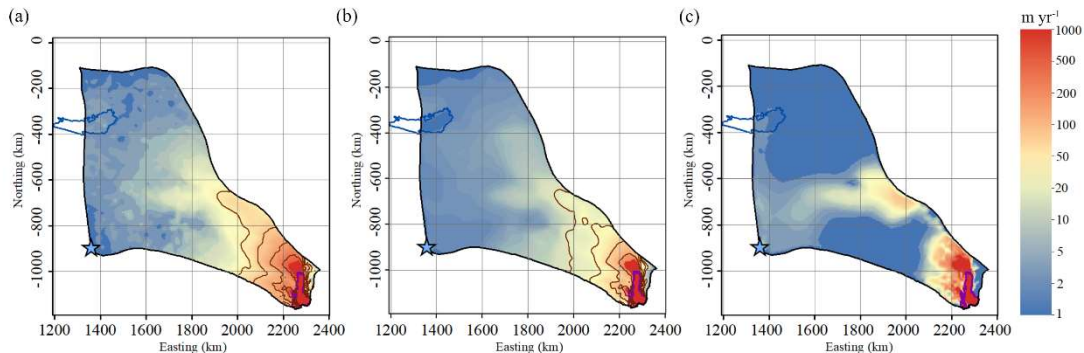

Fig. 4. (a) Observed surface velocity, (b) modeled surface velocity and (c) modeled basal velocity in the experiment using the Martos et al. (2017) GHF. The brown solid lines in (a) and (b) represent speed contours of 30, 50, 100 and 200 m yr^{-1}. The purple line depicts the grounding line. The blue curve depicts Lake Vostok. The blue star denotes Dome C.

4.2 Basal Ice Temperature, Basal Friction Heat and Heat Conduction

Fig. 5 shows the modelled basal temperatures from the ten experiments. In the fast-flowing region (defined as having surface speeds higher than 30 m yr^{-1}), the modelled ice basal temperatures are all at the pressure melting point ("warm"). However, in the slow-flowing region, the modeled ice basal temperature shows large difference between GHF fields. In the experiment using the Martos et al. (2017), Haeger et al. (2022), Stål et al. (2021), and Lösing et al. (2021) GHF (Fig. 5), which has similar high GHF over the domain, we get the largest area of warm base extending to all but the inland southwest corner. The warm bed yielded by the constant GHF is close to the above four GHF, although the constant GHF value is lower than the mean value of any one of the above four GHF (Table 2). The experiment using Shen et al. (2020) GHF (Fig. 5c), which has the moderately high GHF, yields the medium-sized area of warm base. The experiments using An et al. (2015), Shapiro and Ritzwoller (2004) and Purucker (2012) GHF produce slightly less area of warm bed than Shen et al. (2020) GHF. The experiment using Purucker (2012) GHF (Fig. 5b), with the lowest GHF has the smallest

warm base area, which is mostly confined to the fast-flowing region. All experiments show cold basal temperatures in the southwest corner which is associated with relatively thin ice above subglacial mountains (Fig. 1c), and coincide with high values of SD in modelled basal temperature (Fig. 5k). The warm bed area using the ensemble mean GHF is between that by the top four high GHF, and that by Shen et al. (2020) GHF.
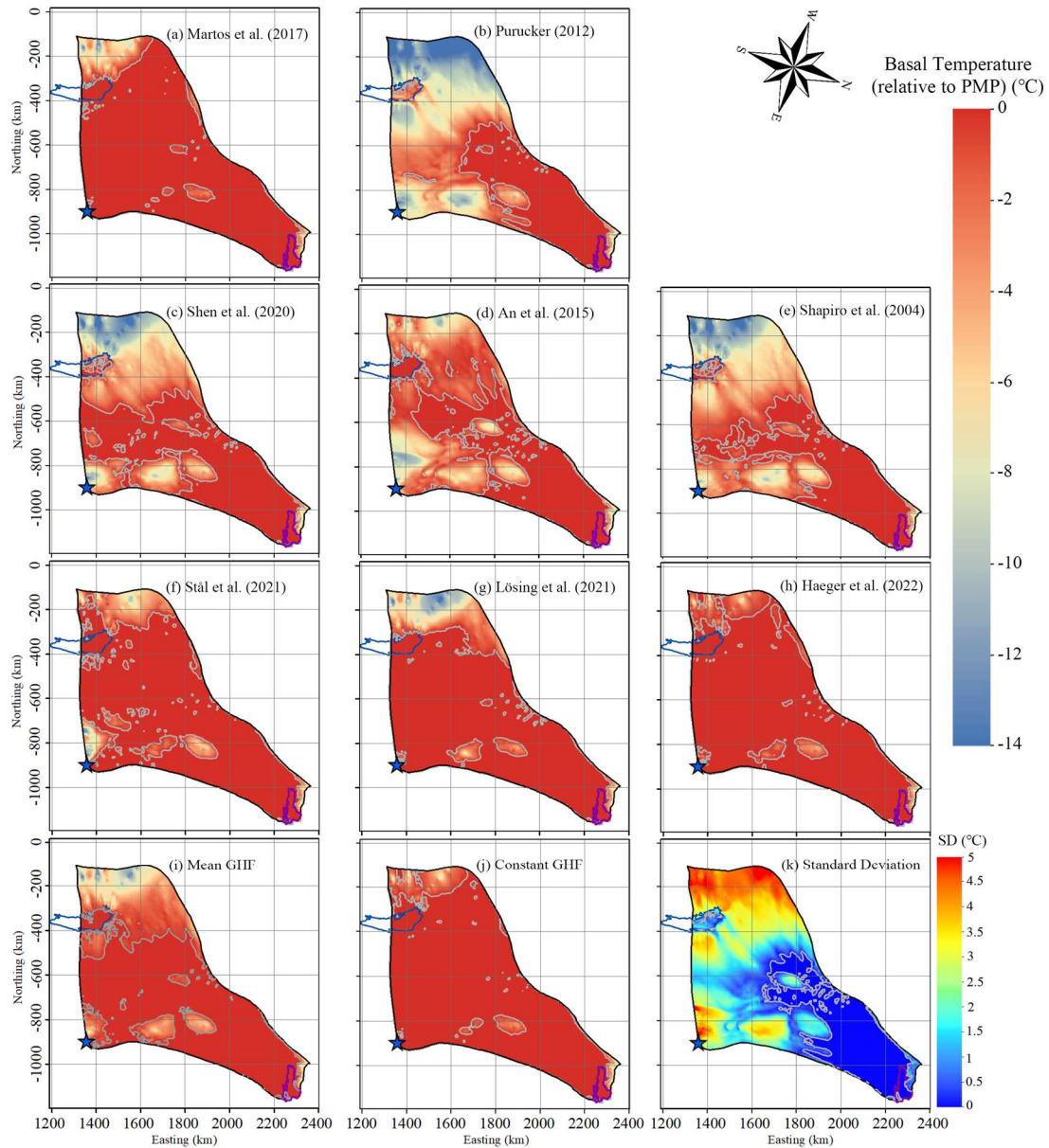
Fig. 5. Modelled basal temperature relative to pressure melting point, (a) to (j) corresponding to the GHF (a) to (j) in Fig. 2. Panel (k) is the standard deviation of 8 modelled basal temperatures (a)-(h). The ice bottom at the pressure-melting point is delineated by a gray contour. The purple line depicts the grounding line. The blue curve depicts Lake Vostok. The blue star denotes Dome C.
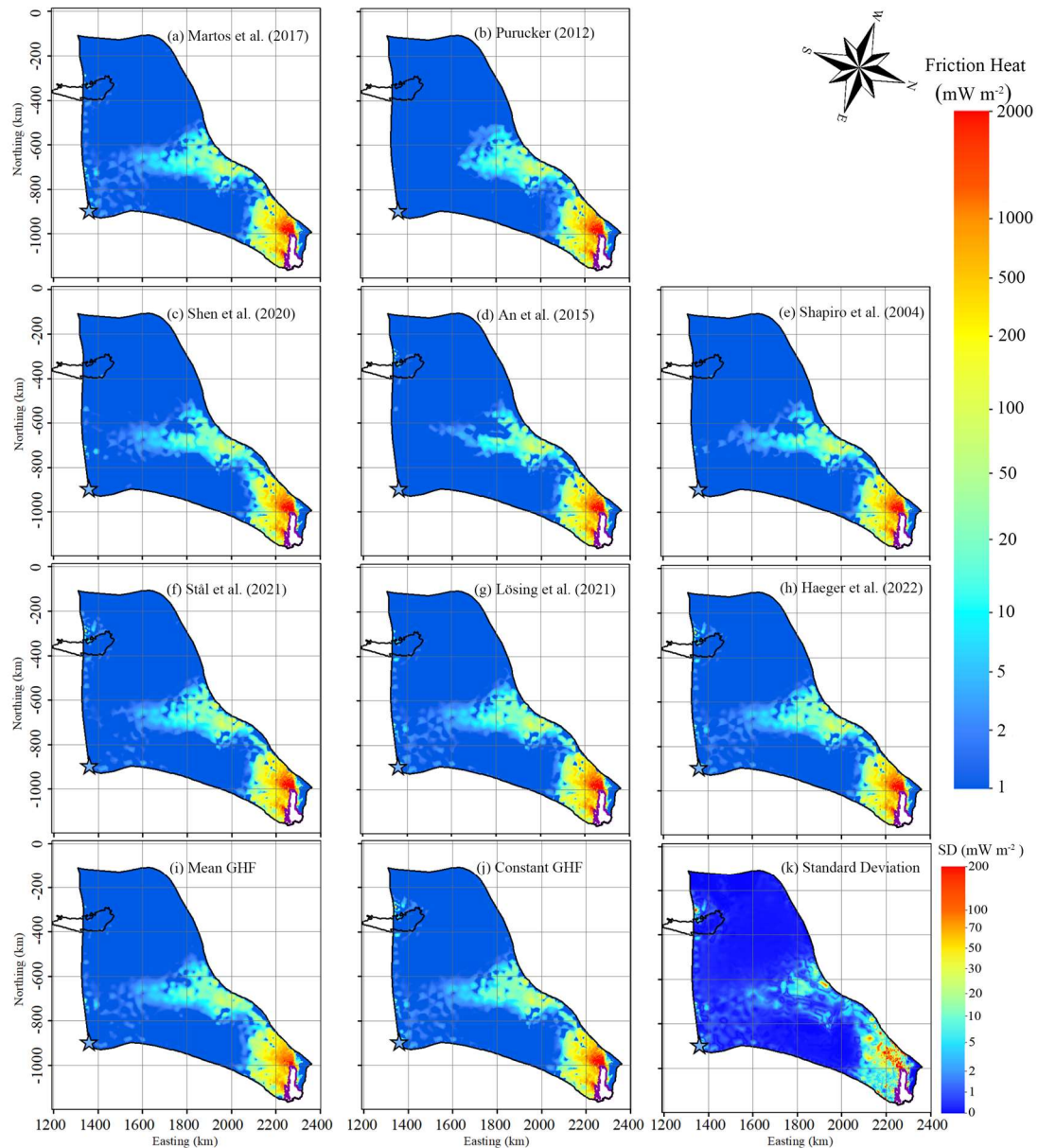
Fig. 6. Modelled basal friction heat, (a) to (j) corresponding to the GHF (a) to (j) in Fig. 2. Panel (k) is the standard deviation of 8 modelled basal friction heat (a)-(h). The purple line depicts the grounding line. The black curve depicts Lake Vostok. The blue star denotes Dome C.

The distribution of modeled basal friction heat is closely associated with that of modelled basal velocity. The patterns of basal friction heat with different GHFs are very similar in fast flow region, but have some differences in the middle of the domain (Fig. 6) where modelled basal velocity ranges between 5-20 m yr^{-1} (Fig. 4).

The modelled basal friction heat is close to 0 where the surface ice velocity is less than 10 m yr^{-1}, but ranges widely by 10-2000 mW m^{-2} with SD between 1 mW m^{-2} and 200 mW m^{-2} in the fast flowing region. Basal friction heating larger than 100 mW m^{-2} occurs where surface velocity is more than 50 m yr^{-1} and basal velocity is higher than 10 m yr^{-1} (Fig. 6; Fig. 4), and it is then the dominant heat source.

11

290

291
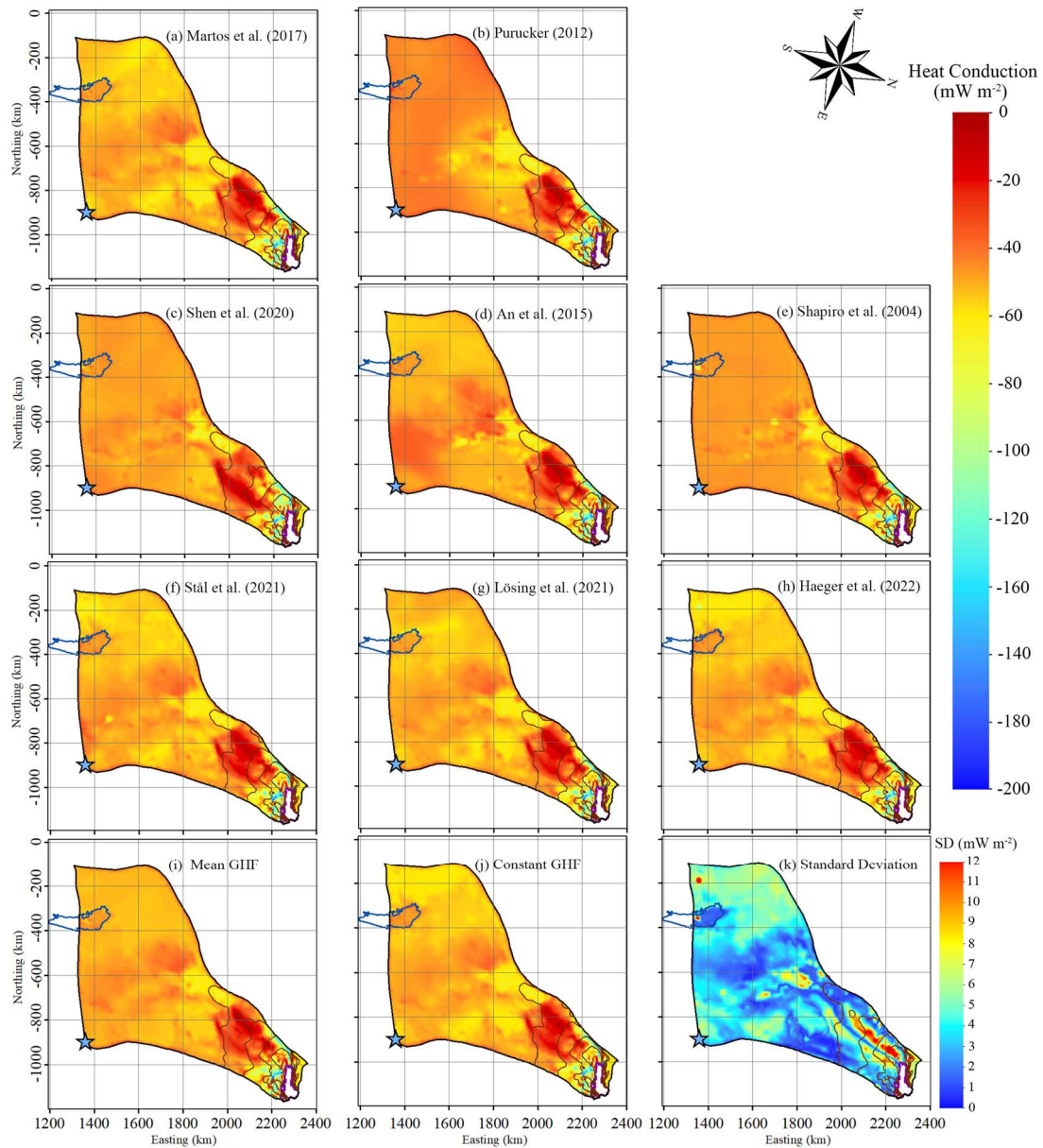
Fig. 7. Modelled heat change of basal ice by upward englacial heat conduction. The negative sign means that the upward englacial heat conduction causes heat loss from the basal ice as defined by the color bar with cooler colors representing more intense heat loss by conduction. (a) to (j) corresponding to the GHF (a) to (j) in Fig. 2. Panel (k) is the standard deviation of 8 modelled basal friction heat (a)-(h). The brown solid curves represent modelled surface speed contours of 30, 50, 100 and 200 m yr^{-1}, as in Fig. 4. The purple line depicts the grounding line. The blue curve depicts Lake Vostok. The blue star denotes Dome C.

300

Fig. 7 shows the modeled heat change of basal ice by upward englacial heat conduction in the ten experiments. In the slow-flowing region where basal temperature is below the pressure melting point, the upward basal heat conduction equals the GHF (Fig. 5, Fig. 7). In the fast-flowing region with thick ice ($\geqslant$2500 m; Fig. 1c), the heat loss

caused by upward basal heat conduction is < 30 mW m^{-2} in all experiments (Fig. 7), reflecting the development of a temperate basal layer that limits the basal thermal gradient. In the fast-flowing tributaries with ice thickness <2000 m, the combination of reduced ice thickness and increased concentration of shear heating at the basal plane rather than in the lower ice column removes the temperate layer and allows very large values of upward basal heat conduction, up to 60-200 mW m^{-2} near the grounding line (Fig. 7).

4.4 Basal Melt Rate

We calculate basal melt rate using the thermal balance equation (Eq 3). There are significant differences in the ten experiments due to large variability in GHF (Fig. 8). The Martos et al. (2017), Haeger et al. (2022), Stål et al. (2021), and Lösing et al. (2021) GHF yield the largest areas with basal melting. The experiments using Shen et al. (2020), An et al. (2015), Shapiro and Ritzwoller (2004) and Purucker (2012) GHF yield less and similar total basal melting areas but have different spatial patterns. The basal melting area produced by the experiment using ensemble mean GHF is between the four large areas and the four small areas. But the basal melting area produced by the constant GHF is larger than that by all the 8 GHF (Fig. 8).

In most of the warm based regions, the modeled basal melting rate is <5 mm yr^{-1} (Fig. 8) and basal friction heat is < 50 mW m^{-2} (Fig. 6). Basal melting rates >5 mm yr^{-1} occur with surface velocities > 100 m yr^{-1} (Fig. 4, Fig. 8), where the basal friction heat is the dominant heat source. In particular, the modeled basal melting rate is 50-400 mm yr^{-1} in the two fast flow tributaries feeding the ice shelf that have surface velocities > 200 m yr^{-1}, and where the basal friction heat can reach 500-2000 mW m^{-2} (Fig. 4, Fig. 6, Fig. 8). This is consistent with the findings of Larour et al. (2012) and Kang et al. (2022), that the slow-flowing ice is more sensitive to GHF while the fast-flowing region is more sensitive to basal friction heat.

There is relatively high modelled basal melt rate (4-10 mm yr^{-1}) localized at the central subglacial canyon (Fig. 8, Fig. 1c), which is captured by all ten GHF experiments, and also consistent with the high values (0.5-1.0) of specularity content data there (Fig. 9). Dow et al. (2020) found that the specularity content is a useful proxy for both water depth and water pressure in regions of distributed water in subglacial canyons.

There is a location with modelled refreezing (negative melting rate) at the central subglacial canyon, near the observed subglacial lake, in all ten GHF experiments (Fig. 8). The value of specularity content there is low as 0-0.1 (Fig. 9), and freeze on is driven by the steep topography around the canyon.
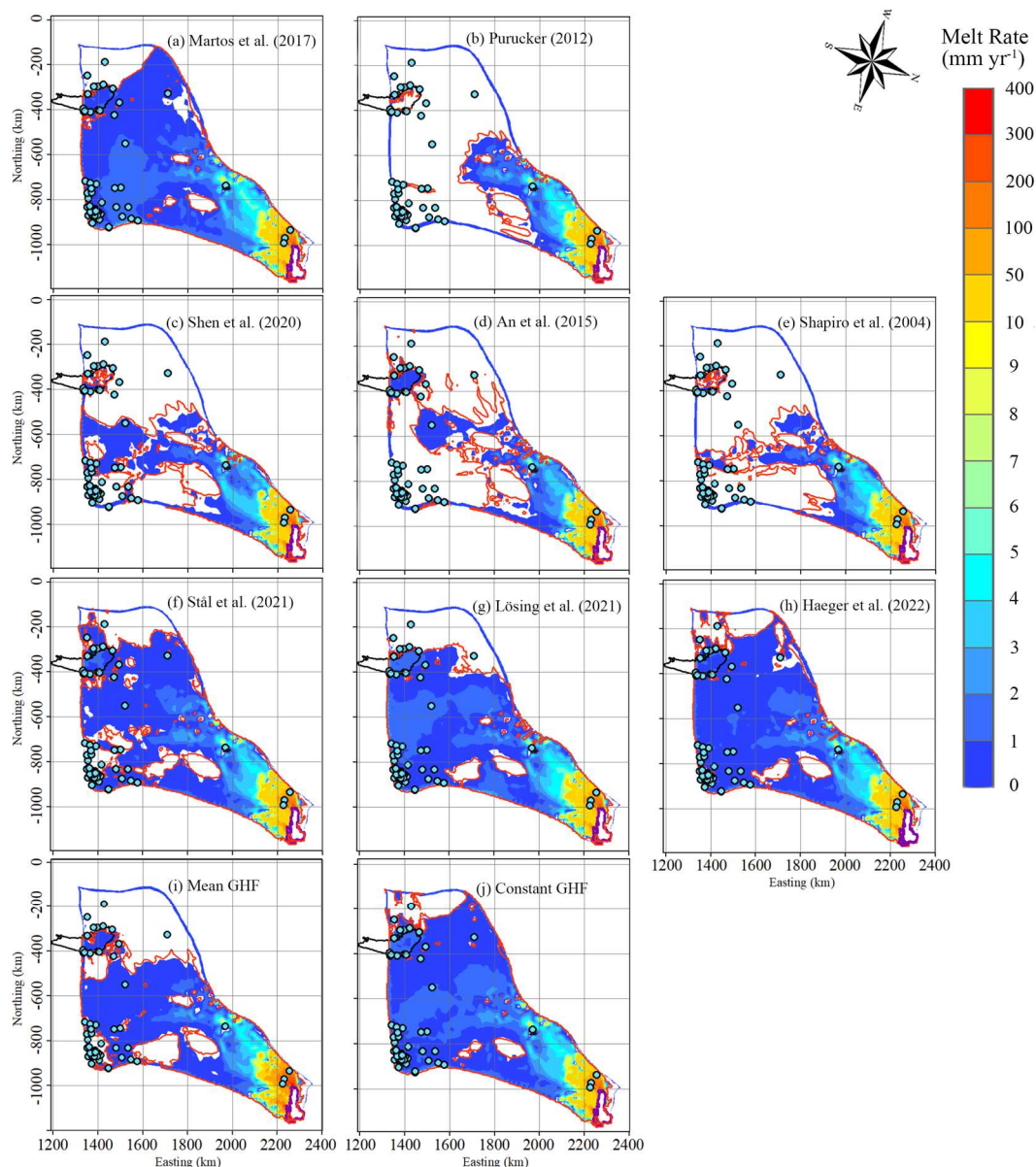
Fig. 8. Modelled basal melt rate, (a) to (j) correspond to the GHF (a) to (j) in Fig. 2. The ice bottom at pressure-melting point is surrounded by a red contour. The black curve depicts Lake Vostok. Stable subglacial lakes are shown as blue-green points with black circles. The purple line depicts the grounding line. There is modelled basal refreezing at the central canyon painted in black.

4.5 Evaluation of modelled results with 8 GHFs

We use the locations of the observed subglacial lakes and specularity content to discriminate between modeled basal melting (Fig. 8). Ideally, we would like to have a modeled ice base that is cold and dry where subglacial lakes do not exist and the specularity content is low, and a modeled ice base that is at the melting point where lakes and high specularity content are observed. In other words, we would like to use the available data to form a two-sided constraint that can penalize the model for being both too warm and too cold. If we only have a one-sided constraint, then we would

359 always end up concluding that either the warmest or the coldest GHF map is best,
360 regardless of whether that map was a reasonable representation of the basal state.
361
362 Observations of subglacial lakes are mostly a one-sided constraint on the basal thermal
363 state. This is because lakes are only detectable if subglacial water accumulates in
364 depressions that are deep compared to the radar wavelength and wide in comparison to
365 the horizontal resolution of the radar system. Other forms of distributed hydrology,
366 such as linked cavities or saturated subglacial sediments, do not produce the classic flat
367 bright reflectors characteristic of subglacial lakes. Thus, the lack of observed subglacial
368 lakes in a particular region cannot be taken as evidence that there is no subglacial water
369 there. The mesh resolution of our model inland is about 20 km (Fig. 3). But 84% of the
370 subglacial lakes have along-radar track lengths below 5 km, 94% are below 10 km, with
371 only 5 lakes including Lake Vostok above 10 km (Fig. 9f). So the subglacial lakes may
372 be too small for the ice model to resolve. Nonetheless, we compare our modeled basal
373 thermal state with the observed locations of subglacial lakes. These comparisons show
374 that all the experiments can capture all four subglacial lakes in the fast-flowing region
375 (Fig. 8). But their performance in covering subglacial lakes in the slow-flowing region
376 differ greatly.
377
378 In addition to the subglacial lakes, we use specularity content to derive a two-sided
379 constraint on basal thermal state. Specularity content is an inherently noisy measure, so
380 it is smoothed to 1 km along track values, and furthermore it is not unambiguously an
381 indicator of wet beds. For example, specularity content is low in the fast-flowing region
382 (Fig. 9, Fig. 4), where there must be lubricating water at the bed. Similar specularity
383 results were also seen by Schroeder et al. (2013) for Thwaites Glacier, where high
384 specularity values are seen under the major tributaries and the upstream trunk, but
385 significant lower values of specularity in the fast-flowing region. This counter-intuitive
386 result may be due to distinct morphologies and radar scattering signatures between
387 water distributed in widespread subglacial conduits and water concentrated in just a few
388 subglacial channels. Because of this effect, we only use the specularity content outside
389 the fast-flowing region (defined as surface speed>30 m a^{-1}, Fig. 9).
390
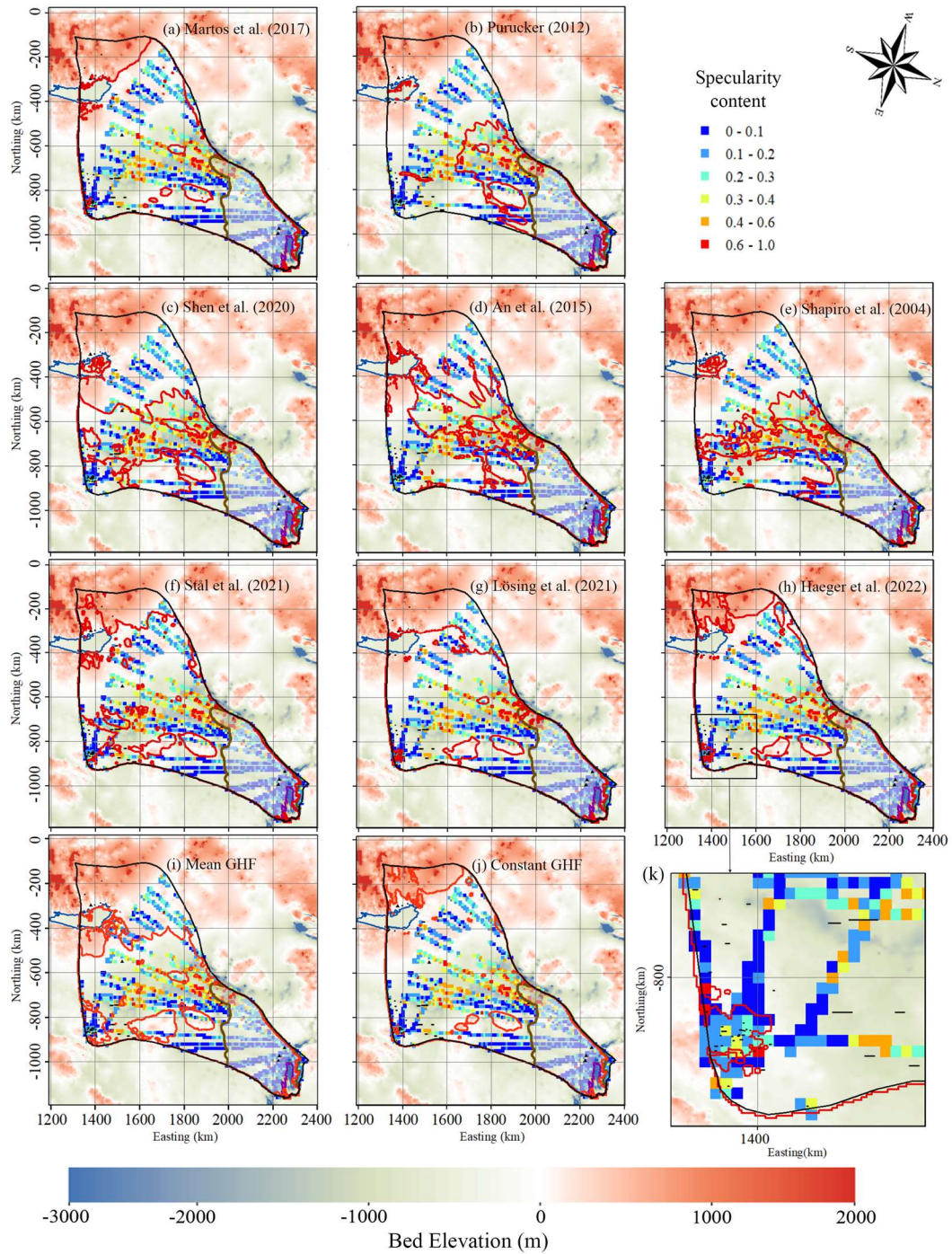
Fig. 9. Locations of specularity content (colored points) derived from radar data collected by ICECAP (Dow et al., 2020) and interpolated to 10 km by 10 km grids under the background of bedrock elevation. Specularity content > 0.4 indicates the likely presence of basal water. The ice bottom at pressure-melting point is surrounded by a red contour, (a) to (j) correspond to the ten GHF maps (a) to (j) in Fig. 2. Lake Vostok is outlined by a blue curve. The brown curve is the contour of surface speed of 30 m a^{-1}. Subglacial lakes are shown at observed positions as a line segment of their length. Plot (k) is a zoom of the box in plot (h).

The specularity content data calculated from ICECAP survey lines suggests hundreds

of locations with basal water (Dow et al., 2020). The default resolution of specularity content along the flight lines is 1 km (Dow et al., 2020), which is smaller than our model resolution of 6-20 km in the slow flowing region. Water may accumulate in just a small fraction of the grid cell even if the majority of the cell is warm because of water flow. For comparability with our simulation resolution we aggregated the specularity content data onto 10 km by 10 km windows (Fig. 9). The 10 km window is a somewhat arbitrary choice, but smaller windows (we tried 2 and 5 km) reduce the data available and noise becomes larger, while larger windows (we tried 15 and 20 km) restrict spatial resolution. We then take the upper fifth percentile of the specularity content, $specularity_5$ of each window as a water indicator rather than its mean value to allow for localized water collection or unfavorable bed reflection geometry, while also excluding spurious signals in the noisy specularity data. Young et al. (2016) suggested that specularity larger than 0.4 was an indicator of a warm bed. This is also consistent with the largest subglacial lake in the domain with length of 28 km having specularity content>0.4 (Fig. 9k). There are also some smaller lakes (several km along-track lengths) with specularity content between 0.2 and 0.4, so a warm threshold of 0.4 would not capture these features. The cold threshold need not be the same as the warm bed one, and so we explored different values for cold thresholds of 0.2, 0.3, 0.4, but found that the 0.2 cold threshold provided best discrimination between models, and also maximizes the available data.

To evaluate modelled basal conditions with specularity content, we define a warm hit rate as the ratio of the number of grid cells with modelled warm bed that have $specularity_5 > 0.4$ to the total number of grids with $specularity_5 > 0.4$. Similarly, cold hit rate is defined as the ratio of the number of grid cells with $specularity_5 < 0.2$.

One simple measure of quality is just the average of warm hit rate and cold hit rate, but we also want an unbiased evaluation of GHF to have similar capabilities in capturing both warm bed and cold bed regions. Therefore, we define *imbalance* as

$$imbalance = \frac{warm\ hit\ rate - cold\ hit\ rate}{warm\ hit\ rate + cold\ hit\ rate},$$

as it reflects the difference between warm hit rate and cold hit rate, and has a value between -1 and 1. The closer to zero *imbalance* is, the more confidence we have in the model result. The overall performance is estimated by averaged hit rate minus the absolute value of *imbalance*.

The constant GHF yields the higher warm hit rate and the lower cold hit rate than any single GHF map since it produces larger warm bed area. The four highest GHF, Martos et al. (2017), Haeger et al. (2022), Stål et al. (2021), and Lösing et al. (2021) GHF have similarly the highest warm hit rate and lowest cold hit rate among the 8 GHF since they have the largest modelled warm bed area. The averaged hit rates of modelled results with 8 GHF are close, with differences < 0.13 (Table 3). The Shapiro and Ritzwoller (2004), Purucker (2012), then Shen et al. (2020) have the highest averaged hit rate using all the values for threshold of cold bed, and the differences between their averaged hit rate < 0.04. The mean GHF has the same averaged hit rate as Shen et al. (2020).

Martos et al. (2017), Haeger et al. (2022), Stål et al. (2021), and Lösing et al. (2021) GHF have large positive *imbalance* >0.5, which means that their warm hit rates overwhelm their cold hit rates. Shen et al. (2020) has positive but near-zero *imbalance*. In contrast, An et al. (2015), Shapiro and Ritzwoller (2004) and Purucker (2012) GHF have negative *imbalance* (Table 3).

Considering the overall performance by averaged hit rate minus the absolute value of *imbalance*, Shen et al. (2020) ranks the first, Shapiro and Ritzwoller (2004) the second, Purucker (2012) the third, An et al. (2015) the fourth, Martos et al. (2017), Stål et al. (2021), Lösing et al. (2021) and Haeger et al. (2022) get negative score, and rank the last four among the 8 GHF (Table 3). The ensemble mean GHF gets score close to An et al. (2015). The constant GHF gets lower score than any GHF. The ranking is robust with all three cold hit thresholds.

Table 3. Warm hit rate, cold hit rate, averaged hit rate, imbalance and overall performance for the modelled results with eight individual GHF maps, ensemble mean GHF, and constant GHF of 58.75 mW m^{-2} in Table 2. The overall performance is calculated by averaged hit rate minus the absolute value of imbalance. The threshold of *specularity$_5$* is taken as 0.4 for warm hit rate, and 0.2 for cold hit rate.

GHF	warm hit rate	cold hit rate	averaged hit rate	Imbalance	overall performance
Martos et al., 2017	0.9560	0.1648	0.56	0.71	-0.15
Purucker, 2012	0.5283	0.8201	0.67	-0.22	0.45
Shen et al., 2020	0.6588	0.6564	0.65	0.0018	0.65
An et al., 2015	0.4340	0.7652	0.60	-0.28	0.32
Shapiro and Ritzwoller, 2004	0.5975	0.7822	0.69	-0.13	0.56
Stål et al., 2021	0.8750	0.2405	0.56	0.57	-0.01
Lösing et al., 2021	0.9313	0.2216	0.58	0.62	-0.04
Haeger et al., 2022	0.9688	0.1458	0.56	0.74	-0.18
Mean GHF	0.8750	0.4205	0.65	0.35	0.30
Constant GHF	0.9813	0.1042	0.54	0.81	-0.27

5 Discussion

Wright et al. (2012) modelled basal temperature of Totten Glacier using the Glimmer ice sheet model with a constant GHF of 54 mW m^{-2}. Their modelled area of basal warm ice is between what we simulated using Martos et al. (2017) and Shen et al. (2020) GHF, covering most of the lakes and lake-like features but missing some near Lake Vostok. Dow et al. (2020) ran the Ice Sheet System Model (Larour et al., 2012) with a constant GHF of 55 mW m^{-2}, producing a warm bed region slightly larger than we simulated using the Shen et al. (2020) GHF (which has a mean of 58 mW m^{-2} in this region, Table

2). However, our experiment with a constant GHF of 59 mW m^{-2} produces warm bed region almost as large as that with Martos et al. (2017) GHF suggesting this constant value is too high for this domain. Our experiment with ensemble mean GHF gives warm bed region close to that by Shen et al. (2020) GHF, indicating ensemble mean is a better choice than the mean of ensemble mean.

Kang et el. (2020) evaluated basal thermal conditions underneath the Lambert-Amery glacier system using six GHFs, and found that the two most recent GHF fields inverted from aerial geomagnetic observations and which have the highest GHF values, produced the largest warm-based area, and best matched the observed distribution of subglacial lakes. This might be expected as there was only a one-sided constraint used, and warm based models produced matches with more lakes.

Although the basal ice in fast-flowing regions is all at pressure melting point because basal friction heat dominates the heat balance, the modelled basal melt rate of the grounded ice in fast-flowing regions exhibits large differences across-models. The modelled basal melt rate is associated with the modelled basal friction heat, which is a function of the modelled basal velocity and basal shear stress, the accuracy of which depends on the configuration and constraints of the ice sheet model used. Our modelled maximum basal melt rate on the grounded ice is 0.4 m yr^{-1} near the grounding line. This is close to the modelled maximum basal melt rate of 0.34 m yr^{-1} near the grounding line by Dow et al. (2020), where they calculated the basal melt rates as a function of combined GHF and frictional heating using the Ice Sheet System Model. We know of no observations of the basal melt rates of grounded ice in Totten Glacier.

Modelled basal sliding speeds by Dow et al. (2020) range from 0.06 m yr^{-1} inland to 900 m yr^{-1} at the grounding line, which is close to our result (Fig. 4). Dow et al (2020) simulate basal sliding generally where bedrock is below sea level, with an area close to our simulation with a basal sliding coefficient β_{old} and which is larger than ours using the improved basal sliding coefficient β_{new} (Eq 2) found by considering the basal temperature relative to pressure-melting point. The modelled basal sliding speed reaches a local maximum at the middle of the subglacial canyon system (Fig. 4), which leads to local maxima in basal friction and basal melt rate (Fig. 8), and is consistent with the high values of specularity (Fig. 9).

To evaluate the simulation results, we compare the simulated basal melting area with the locations of the discovered subglacial lakes and specularity content derived from radar data collected by ICECAP (Dow et al., 2020). Specularity is a parameterization that estimates the along-track angularly narrow component of bed echo energy compared with the isotropic diffuse energy component (Schroeder et al., 2015). Specularity is determined by a set of ice/bed properties including the length, width and thickness of the water body, its conductivity, and the roughness of the ice/water interface. Off-nadir across-track reflectors may also produce glints creating noise in the specularity distribution. Hence, interpretation of specularity is ambiguous and

dependent on the local bed morphology. This led us to experiment with a range of windows over which to aggregate the bed reflection energy, and various thresholds for estimating cold and warm beds. We were able to use the numerous subglacial lakes in the region as a guide to setting these parameters, bearing in mind that the observations of subglacial lakes are a one-sided constraint. If the modeled basal melting area misses the subglacial lake or high specularity content, the model is underestimating the basal temperature at that location. However, if the basal melting is simulated in areas without observed subglacial lakes, it is unclear if this is because the models overestimate the temperature in those areas, or if the water under the ice sheet has not been detected. In addition, relatively high electrical conductivity beds like water saturated clays can lead to false positives in radar detections of subglacial water bodies (Talalay et al., 2020).

Our evaluation using specularity content is a two-sided constraint and thus improves on observed subglacial lakes as a discriminating feature of cold and warm beds. Using subglacial lakes as a one-sided constraint, Haeger et al., (2022) and Martos et al. (2017) GHF rank the top two as they model the largest region of basal melt, however, they ranks the last two using specularity content as a two-sided constraint because it cannot capture cold beds well.

6 Conclusions

In this study we diagnose the basal thermal state of Totten Glacier by coupling a forward model and an inverse model and using eight different GHFs. By comparing modelled basal temperature distributions with metrics derived from specularity content data we evaluate the reliability of the eight GHF data in this area.

We find there are significant differences in the spatial distributions of modelled temperate ice with different GHFs, and the differences are mainly concentrated in the slow ice flow regions. The modelled basal thermal state (frozen/melting) in the slow ice flow region is mainly determined by the heat balance between GHF and englacial upward heat conduction, and the basal melting rate is generally less than 5 mm yr^{-1}. However, there is local maximum in modelled basal melt rate (4-10 mm yr^{-1}) at the central subglacial canyon, which could be explained by the local high basal sliding velocity and frictional heat that are captured by all GHF experiments. This is consistent with the high values of specularity content data there.

The basal heat balance in the fast ice flow region is mainly determined by the basal frictional heat. The basal ice in the fast flow region is all at the melt point. The modeled basal melting rate is 50-400 mm yr^{-1} in the two fast flow tributaries feeding the ice shelf with surface velocity greater than 200 m yr^{-1}, where the basal friction heat is 500-2000 mW m^{-2}.

Our evaluation using specularity content as a two-sided constraint, gives quite different result than only using observed locations of subglacial lakes. Simulations with the Martos et al. (2017), Haeger et al., (2022), Stål et al. (2021), and Lösing et al. (2021)

GHF yield the largest region of basal melt, which covers most observed subglacial lake locations, however, their cold bed fit with specularity content is poor and shows huge imbalance in modelling warm bed and cold bed regions. Overall, Martos et al. (2017), Haeger et al., (2022), Stål et al. (2021), and Lösing et al. (2021) GHF rank last in the evaluation with specularity content. The constant GHF, area average of ensemble mean of the eight GHF produces a lower score than any of the eight individual GHF maps. The ensemble mean GHF gets the middle ranks. Shen et al. (2020) GHF yields the second largest area of basal melt and second best agreement with the locations of the subglacial lakes, and also scores well in modelling both warm and cold bed areas. Shen et al. (2020) GHF and Shapiro and Ritzwoller (2004) GHF rank the top two according to the evaluation with specularity content. The best-fit simulated result shows that most of the inland bed area is frozen. Only the upstream subglacial canyon inland reaches pressure-melting point, and modelled basal melting rate there is 0-10 mm yr^{-1}.

Data availability

MEaSUREs BedMachine Antarctica, version 2, is available at https://doi.org/10.5067/E1QL9HFQ7A8M (Morlighem, 2020). MEaSUREs InSAR-based Antarctic ice velocity Map, version 2, is available at https://doi.org/10.5067/D7GK8F5J8M8R (Rignot et al., 2017). MEaSUREs Antarctic Boundaries for IPY 2007–2009 from Satellite Radar, version 2 is available at https://doi.org/10.5067/AXE4121732AD (Mouginot et al., 2017). The subglacial lake dataset is available at https://doi.org/10.1038/s43017-021-00246-9 (Livingstone et al., 2022). The specularity content dataset https://doi.org/10.5281/zenodo.3525474 (Dow et al., 2020). ALBMAP v1 and the GHF dataset of Shapiro and Ritzwoller (2004) are available at https://doi.org/10.1594/PANGAEA.734145 (Le Brocq et al., 2010b). The GHF dataset of An et al. (2015) is available at http://www.seismolab.org/model/antarctica/lithosphere/AN1-HF.tar.gz (last access: 11 April 2023). The GHF dataset of Shen et al. (2020) is available at https://sites.google.com/view/weisen/research-products?authuser=0 (last access: 11 April 2023). The GHF dataset of Martos (2017) is available at https://doi.org/10.1594/PANGAEA.882503. The GHF dataset of Purucker (2012) is available at http://websrv.cs.umt.edu/isis/index.php/Antarctica_Basal_Heat_Flux (last access: 11 April 2023). The modelled basal temperature, basal melt rate and the upper fifth percentile of the specularity content in this paper will be available at https://doi.org/10.5281/zenodo.7825456.

Author contributions.

LZ and JCM conceived the study. LZ, MW, and JCM designed the methodology. YH, LZ, and YM carried out the simulations and produced the estimates and figures. LZ wrote the original draft, and all the authors revised the paper.

Competing interests.

The authors declare no conflict of interest.

References

Adusumilli, S., Fricker, H. A., Medley, B., Padman, L., and Siegfried, M. R.: Interannual variations in meltwater input to the Southern Ocean from Antarctic ice shelves, Nat. Geosci., 13, 616–620, https://doi.org/10.1038/s41561-020-0616-z, 2020.

An, M., Wiens, D. A., Zhao, Y., Feng, M., Nyblade, A., Kanao, M., Li, Y., Maggi, A., and Lévêque, J.: Temperature, lithosphere-asthenosphere boundary, and heat flux beneath the Antarctic Plate inferred from seismic velocities, J. Geophys. Res.-Sol. Ea., 120, 359–383, https://doi.org/10.1002/2015JB011917, 2015.

Bell, R. E., Studinger, M., Shuman, C. A., Fahnestock, M. A., and Joughin, I.: Large subglacial lakes in East Antarctica at the onset of fast-flowing ice streams, Nature, 445, 904–907, https://doi.org/10.1038/nature05554, 2007.

Bullard, E. C.: The disturbance of the temperature gradient in the earth's crust by inequalities of height, Geophysical Supplements, Mon. Not. R. Astron. Soc., 4, 360–362, https://doi.org/10.1111/j.1365-246X.1938.tb01760.x, 1938.

Colgan, W., MacGregor, J. A., Mankoff, K. D., Haagenson, R., Rajaram, H., Martos, Y. M., Morlighem, M., Fahnestock, M. A., and Kjeldsen, K. K.: Topographic correction of geothermal heat flux in Greenland and Antarctica, J. Geophys. Res.-Earth, 126, e2020JF005598, https://doi.org/10.1029/2020JF005598, 2021.

Comiso, J. C.: Variability and Trends in Antarctic Surface Temperatures from In Situ and Satellite Infrared Measurements, J. Climate, 13, 1674–1696, https://doi.org/10.1175/1520-0442(2000)013<1674:VATIAS>2.0.CO;2, 2000.

Dow, C. F., McCormack, F. S., Young, D. A., Greenbaum, J. S., Roberts, J. L., and Blankenship, D. D.: Totten Glacier subglacial hydrology determined from geophysics and modeling, Earth Planet. Sc. Lett., 531, 115961, https://doi.org/10.1016/j.epsl.2019.115961, 2020.

Dow, Christine. Aurora Subglacial Basin GlaDs inputs, outputs and geophysical data [data set]. Zenodo. https://doi.org/10.5281/zenodo.3525474, 2019.

Fox Maule, C., Purucker, M. E., Olsen, N., and Mosegaard, K.: Heat flux anomalies in Antarctica revealed by satellite magnetic data, Science, 309, 464–467, https://doi.org/10.1126/science.1106888, 2005.

Fricker, H. A., Siegfried, M. R., Carter, S. P., and Scambos, T. A.: A decade of progress in observing and modelling Antarctic subglacial water systems, Phil. Trans. R. Soc. A., 374, 20140294, https://doi.org/10.1098/rsta.2014.0294, 2016.

Gagliardini, O., Zwinger, T., Gillet-Chaulet, F., Durand, G., Favier, L., de Fleurian, B., Greve, R., Malinen, M., Martín, C., Råback, P., Ruokolainen, J., Sacchettini, M., Schäfer, M., Seddik, H., and Thies, J.: Capabilities and performance of Elmer/Ice, a new-generation ice sheet model, Geosci. Model Dev., 6, 1299–1318,

https://doi.org/10.5194/gmd-6-1299-2013, 2013.

Geuzaine, C. and Remacle, J.-F.: Gmsh: A 3-D finite element mesh generator with built-in pre- and post-processing facilities, Int. J. Numer. Meth. Eng., 79, 1309–1331, https://doi.org/10.1002/nme.2579, 2009.

Gillet-Chaulet, F., Gagliardini, O., Seddik, H., Nodet, M., Durand, G., Ritz, C., Zwinger, T., Greve, R., and Vaughan, D. G.: Greenland ice sheet contribution to sea-level rise from a new-generation ice-sheet model, The Cryosphere, 6, 1561–1576, https://doi.org/10.5194/tc-6-1561-2012, 2012.

Greve, R. and Blatter, H.: Dynamics of Ice Sheets and Glaciers, Advances in Geophysical and Environmental Mechanics and Mathematics, Series Editor: Hutter, K., Springer, ISBN 978-3-642-03414-5, 2009.

Haeger, C., Petrunin, A. G., and Kaban, M. K.: Geothermal heat flow and thermal structure of the Antarctic lithosphere, Geochemistry, Geophysics, Geosystems, 23, e2022GC010501, https:// doi.org/10.1029/2022GC010501, 2022.

Huybrechts, P.: A 3-D model for the Antarctic ice sheet: a sensitivity study on the glacial-interglacial contrast, Climate Dynamics, 5, 79-92, https://doi.org/10.1007/BF00207423, 1990.

Kang, H., Zhao, L., Wolovick, M., and Moore, J. C.: Evaluation of six geothermal heat flux maps for the Antarctic Lambert–Amery glacial system, The Cryosphere, 16, 3619–3633, https://doi.org/10.5194/tc-16-3619-2022, 2022.

Larour, E., Morlighem, M., Seroussi, H., Schiermeier, J., and Rignot, E.: Ice flow sensitivity to geothermal heat flux of Pine Island Glacier, Antarctica, J. Geophys. Res.-Earth, 117, F04023, https://doi.org/10.1029/2012jf002371, 2012.

Le Brocq, A. M., Payne, A. J., and Vieli, A.: An improved Antarctic dataset for high resolution numerical ice sheet models (ALBMAP v1), Earth Syst. Sci. Data, 2, 247–260, https://doi.org/10.5194/essd-2-247-2010, 2010a.

Le Brocq, A. M., Payne, A. J., and Vieli, A.: Antarctic dataset in NetCDF format, PANGAEA [data set], https://doi.org/10.1594/PANGAEA.734145, 2010b.

Li, X., Rignot, E., Mouginot, J., and Scheuchl, B.: Ice flow dynamics and mass loss of Totten Glacier, East Antarctica, from 1989 to 2015, Geophys. Res. Lett., 43, 6366–6373, https://doi.org/10.1002/2016GL069173, 2016.

Livingstone, S. J., Utting, D. J., Ruffell, A., Clark, C. D., Pawley, S., Atkinson, N., and Fowler, A. C.: Discovery of relict subglacial lakes and their geometry and mechanism of drainage, Nat Commun, 7, ncomms11767, https://doi.org/10.1038/ncomms11767, 2016.

Livingstone, S. J., Li, Y., Rutishauser, A., Sanderson, R. J., Winter, K., Mikucki, J. A., Björnsson, H., Bowling, J. S., Chu, W., Dow, C. F., Fricker, H. A., McMillan, M., Ng, F. S. L., Ross, N., Siegert, M. J., Siegfried, M., and Sole, A. J.: Subglacial lakes and their changing role in a warming climate, Nat Rev Earth Environ, 3, 106–124, https://doi.org/10.1038/s43017-021-00246-9, 2022.

Lösing, M., and Ebbing, J.: Predicting geothermal heat flow in Antarctica with a machine learning approach, J. Geophys. Res.-Earth, 126, e2020JB021499, https://doi. org/10.1029/2020JB021499, 2021.

Martos, Y. M.: Antarctic geothermal heat flux distribution and estimated Curie Depths,

693   links to gridded files, PANGAEA [data set],
694   https://doi.org/10.1594/PANGAEA.882503, 2017.

695 Martos, Y. M., Catalán, M., Jordan, T. A., Golynsky, A., Golynsky, D., Eagles, G., and
696   Vaughan, D. G.: Heat Flux Distribution of Antarctica Unveiled, Geophys. Res.
697   Lett., 44, 11,417-11,426, https://doi.org/10.1002/2017GL075609, 2017.

698 Morlighem, M.: MEaSUREs BedMachine Antarctica, Version 2, Boulder, Colorado
699   USA, NASA National Snow and Ice Data Center Distributed Active Archive
700   Center [data set], https://doi.org/10.5067/E1QL9HFQ7A8M, 2020.

701 Morlighem, M., Rignot, E., Binder, T., Blankenship, D., Drews, R., Eagles, G., Eisen,
702   O., Ferraccioli, F., Forsberg, R., Fretwell,P., Goel,V., Greenbaum, J. S.,
703   Gudmundsson, H., Guo, J., Helm,V., Hofstede, C., Howat, I., Humbert, A., Jokat,
704   W., Karlsson, N. B., Lee, W., Matsuoka, K., Millan, R., Mouginot, J., Paden,J.,
705   Pattyn, F., Roberts, J., Rosier, S., Ruppel, A., Seroussi, H., Smith, E. C., Steinhage,
706   D., Sun, B., Van den Broeke, M. R., Van Ommen, T. D., Van Wessem, M., and
707   Young D. A.: Deep glacial troughs and stabilizing ridges unveiled beneath the
708   margins of the Antarctic ice sheet, Nat. Geosci., 13, 132–137,
709   https://doi.org/10.1038/s41561-019-0510-8, 2020.

710 Mouginot, J., Scheuchl, B., and Rignot, E.: MEaSUREs Antarctic Boundaries for IPY
711   2007-2009 from Satellite Radar, Version 2, National Snow and Ice Data Center
712   [data set], https://doi.org/doi.org/10.5067/AXE4121732AD, 2017.

713 Pattyn, F.: Antarctic subglacial conditions inferred from a hybrid ice sheet/ice stream
714   model, Earth Planet. Sc. Lett., 295, 451–461,
715   https://doi.org/10.1016/j.epsl.2010.04.025, 2010.

716 Pittard, M., Roberts, J., Galton-Fenzi, B., and Watson, C.: Sensitivity of the Lambert-
717   Amery glacial system to geothermal heat flux, Ann. Glaciol., 57, 56–68,
718   https://doi.org/10.1017/aog.2016.26, 2016.

719 Pollack, H. N., Hurter, S. J., and Johnson, J. R.: Heat flow from the Earth's interior:
720   Analysis of the global data set, Rev. Geophys., 31, 267,
721   https://doi.org/10.1029/93RG01249, 1993.

722 Pritchard, H. D., Arthern, R. J., Vaughan, D. G., and Edwards, L. A.: Extensive dynamic
723   thinning on the margins of the Greenland and Antarctic ice sheets, Nature, 461,
724   971–975, https://doi.org/10.1038/nature08471, 2009.

725 Purucker, M.: Geothermal heat flux data set based on low resolution observations
726   collected by the CHAMP satellite between 2000 and 2010, and produced from the
727   MF-6 model following the technique described in Fox Maule et al. (2005), Inter-
728   active System for Ice sheet Simulation [data set],
729   http://websrv.cs.umt.edu/isis/index.php/Antarctica_Basal_Heat_Flux (last access:
730   11 April 2023), 2012.

731 Reading, A.M., Stål, T., Halpin, J.A. , Lösing, M., Ebbing, J., Shen, W., McCormack,
732   F.S., Siddoway, C. S., and Hasterok, D.: Antarctic geothermal heat flow and its
733   implications for tectonics and ice sheets, Nat Rev Earth Environ, 3, 814–831,
734   https://doi.org/10.1038/s43017-022-00348-y, 2022.

735 Roberts, J., Galton-Fenzi, B. K., Paolo, F. S., Donnelly, C., Gwyther, D. E., Padman, L.,
736   Young, D., Warner, R., Greenbaum, J., Fricker, H. A., Payne, A. J., Cornford, S.,

Le Brocq, A., Van Ommen, T., Blankenship, D., and Siegert, M. J.: Ocean forced variability of Totten Glacier mass loss, SP, 461, 175–186, https://doi.org/10.1144/SP461.6, 2018.

Schroeder, D. M., Blankenship, D. D., and Young, D. A.: Evidence for a water system transition beneath Thwaites Glacier, West Antarctica, Proc. Natl. Acad. Sci. U.S.A., 110, 12225–12228, https://doi.org/10.1073/pnas.1302828110, 2013.

Schroeder, D. M., Blankenship, D. D., Raney, R. K., and Grima, C.: Estimating Subglacial Water Geometry Using Radar Bed Echo Specularity: Application to Thwaites Glacier, West Antarctica, IEEE Geosci. Remote Sensing Lett., 12, 443–447, https://doi.org/10.1109/LGRS.2014.2337878, 2015.

Shapiro, N. M. and Ritzwoller, M. H.: Inferring surface heat flux distributions guided by a global seismic model: particular application to Antarctica, Earth Planet. Sc. Lett., 223, 213–224, https://doi.org/10.1016/j.epsl.2004.04.011, 2004.

Shen, W., Wiens, D. A., Lloyd, A. J., and Nyblade, A. A.: A geothermal heat flux map of Antarctica empirically constrained by seismic structure, Geophys. Res. Lett., 47, e2020GL086955, https://doi.org/10.1029/2020gl086955, 2020.

Stål, T., Reading, A. M., Halpin, J. A., and Whittaker, J. M.: Antarctic geothermal heat flow model: Aq1, Geochemistry, Geophysics, Geosystems, 22, e2020GC009428, https://doi. org/10.1029/2020GC009428, 2021.

Studinger, M., Bell, R. E., Karner, G. D., Tikku, A. A., Holt, J. W., Morse, D. L., Richter, T. G., Kempf, S. D., Peters, M. E., Blankenship, D. D., Sweeney, R. E., and Rystrom, V. L.: Ice cover, landscape setting, and geological framework of Lake Vostok, East Antarctica, Earth Planet. Sc. Lett., 205, 195–210, https://doi.org/10.1016/S0012-821X(02)01041-5, 2003.

Talalay, P., Li, Y., Augustin, L., Clow, G. D., Hong, J., Lefebvre, E., Markov, A., Motoyama, H., and Ritz, C.: Geothermal heat flux from measured temperature profiles in deep ice boreholes in Antarctica, The Cryosphere, 14, 4021–4037, https://doi.org/10.5194/tc-14-4021-2020, 2020.

Van Liefferinge, B. and Pattyn, F.: Using ice-flow models to evaluate potential sites of million year-old ice in Antarctica, Clim. Past, 9, 2335–2345, https://doi.org/10.5194/cp-9-2335-2013, 2013.

Van Liefferinge, B., Pattyn, F., Cavitte, M. G. P., Karlsson, N. B., Young, D. A., Sutter, J., and Eisen, O.: Promising Oldest Ice sites in East Antarctica based on thermodynamical modelling, The Cryosphere, 12, 2773–2787, https://doi.org/10.5194/tc-12-2773-2018, 2018.

Wolovick, M. J., Moore, J. C., and Zhao, L.: Joint inversion for surface accumulation rate and geothermal heat flow from ice-penetrating radar observations at Dome A, East Antarctica. Part I: model description, data constraints, and inversion results, J. Geophys. Res.-Earth, 126, e2020JF005937, https://doi.org/10.1029/2020JF005937, 2021.

Wright, A. and Siegert, M.: A fourth inventory of Antarctic subglacial lakes, Antarctic Science, 24, 659–664, https://doi.org/10.1017/S095410201200048X, 2012.

Wright, A. P., Young, D. A., Roberts, J. L., Schroeder, D. M., Bamber, J. L., Dowdeswell, J. A., Young, N. W., Le Brocq, A. M., Warner, R. C., Payne, A. J., Blankenship, D.

781   D., Van Ommen, T. D., and Siegert, M. J.: Evidence of a hydrological connection
782   between the ice divide and ice sheet margin in the Aurora Subglacial Basin, East
783   Antarctica, J. Geophys. Res., 117, 2011JF002066,
784   https://doi.org/10.1029/2011JF002066, 2012.

785 Young, D. A., Schroeder, D. M., Blankenship, D. D., Kempf, S. D., and Quartini, E.:
786   The distribution of basal water between Antarctic subglacial lakes from radar
787   sounding, Phil. Trans. R. Soc. A., 374, 20140297,
788   https://doi.org/10.1098/rsta.2014.0297, 2016.

789 Zhao, C., Gladstone, R. M., Warner, R. C., King, M. A., Zwinger, T., and Morlighem,
790   M.: Basal friction of Fleming Glacier, Antarctica – Part 1: Sensitivity of inversion
791   to temperature and bedrock uncertainty, The Cryosphere, 12, 2637–2652,
792   https://doi.org/10.5194/tc-12-2637-2018, 2018.

793